Geophysical Journal International

Geophys. J. Int. (2015) **202,** 514–528 doi: 10.1093/gji/ggv160
GJI Seismology

Stress-drop heterogeneity within tectonically complex regions: a case study of San Gorgonio Pass, southern California

T.H.W. Goebel,[1] E. Hauksson,[1] P.M. Shearer[2] and J.P. Ampuero[1]

[1]*Caltech Seismological Laboratory, Pasadena, CA* 91125, *USA. E-mail: thw.goebel@gmail.com*
[2]*Scripps Institution of Oceanography, University of California, San Diego, La Jolla, CA* 92037, *USA*

Accepted 2015 April 13. Received 2015 April 12; in original form 2014 October 28

SUMMARY

In general, seismic slip along faults reduces the average shear stress within earthquake source regions, but stress drops of specific earthquakes are observed to vary widely in size. To advance our understanding of variations in stress drop, we analysed source parameters of small-magnitude events in the greater San Gorgonio area, southern California. In San Gorgonio, the regional tectonics are controlled by a restraining bend of the San Andreas fault system, which results in distributed crustal deformation, and heterogeneous slip along numerous strike-slip and thrust faults. Stress drops were estimated by fitting a Brune-type spectral model to source spectra obtained by iteratively stacking the observed amplitude spectra. The estimates have large scatter among individual events but the median of event populations shows systematic, statistically significant variations. We identified several crustal and faulting parameters that may contribute to local variations in stress drop including the style of faulting, changes in average tectonic slip rates, mineralogical composition of the host rocks, as well as the hypocentral depths of seismic events. We observed anomalously high stress drops ($>$20 MPa) in a small region between the traces of the San Gorgonio and Mission Creek segments of the San Andreas fault. Furthermore, the estimated stress drops are higher below depths of $\sim$10 km and along the San Gorgonio fault segment, but are lower both to the north and south away from San Gorgonio Pass, showing an approximate negative correlation with geologic slip rates. Documenting controlling parameters of stress-drop heterogeneity is important to advance regional hazard assessment and our understanding of earthquake rupture processes.

Key words: Fourier analysis; Earthquake source observations; Seismicity and tectonics; Dynamics and mechanics of faulting; Dynamics: seismotectonics.

1 INTRODUCTION

The relative motion of tectonic plates generally causes stress to build-up along systems of faults. These stresses are released during earthquakes. The spatial variations in absolute stresses during earthquakes can generally not be determined directly, however, the relative decrease in shear stress can be estimated from the fault dimensions and slip magnitude. For earthquakes inaccessible to direct observation, stress drops can be estimated from their radiated seismic spectrum by making a number of modelling assumptions. These approaches often begin by deconvolving the seismic record into source, site and path effects. The seismic moment and corner frequency of the source spectrum can be used to determine rupture dimensions and stress drops by assuming a specific model for the fault geometry and rupture dynamics (e.g. Eshelby 1957; Knopoff 1958; Brune 1970; Sato & Hirasawa 1973; Madariaga 1976; Boatwright *et al.* 1991; Kaneko & Shearer 2014).

1.1 Earthquake scaling relations and self-similarity

A detailed description of source parameter variations informs our understanding of earthquake physics including expected ground motions (e.g. Hanks & McGuire 1981) and scaling relations (e.g. Hanks & Thatcher 1972; Prieto *et al.* 2004; Walter *et al.* 2006). High-stress-drop events radiate more high-frequency energy than low-stress-drop events of the same size (i.e. moment), which has large implications for the expected ground motion of a particular sized earthquake (e.g. Hanks 1979; Hanks & McGuire 1981; Heaton *et al.* 1986).

Some studies of source parameter scaling relations indicate self-similar scaling between corner frequencies and moments for regional data sets and mining-induced seismicity (e.g. Abercrombie 1995; Ide & Beroza 2001; Prieto *et al.* 2004; Baltay *et al.* 2010; Kwiatek *et al.* 2011) whereas other studies highlight deviation from self-similarity on regional and global scales (e.g. Kanamori *et al.* 1993; Harrington & Brodsky 2009; Lin *et al.* 2012). Self-similar

earthquake scaling implies that stress drops remain constant and fault slip increases as a function of rupture area (e.g. Prieto *et al.* 2004; Shearer 2009), in which case the physical processes involved in small- and large-magnitude earthquakes are inherently similar (e.g. Aki 1981). The assessment of earthquake stress drops over a range of magnitudes is complicated by near-surface attenuation. Attenuation is especially problematic for small events and high frequencies, which can cause an artificial breakdown of self-similar scaling (Abercrombie 1995). Uncertainties in attenuation corrections, limited recording bandwidths and low-quality records hamper resolution of the controversy regarding possible self-similar source parameter scaling.

1.2 Fault properties, crustal parameters and stress-drop variations

Stress drops are likely influenced by local crustal conditions. For example near Parkfield, seismic off-fault events show largely self-similar scaling whereas some events on the San Andreas fault exhibit the same source pulse width, independent of event magnitudes resulting in stress-drop variations between 0.18 and 63 MPa (Harrington & Brodsky 2009). High stress drops for on-fault events at Parkfield were also suggested by Nadeau & Johnson (1998), although this result was questioned by later studies that suggested stress-drop variations in Parkfield to be comparable to other areas (Sammis & Rice 2001; Allmann & Shearer 2007). In southern California, a comprehensive study of *P*-wave spectra from over 60 000 earthquakes found no correlation between stress drop and distance from major faults (Shearer *et al.* 2006), while a study of global earthquakes with $M>5$ revealed higher stress drops for intraplate compared to plate boundary events (Allmann & Shearer 2009). Elevated stress drops for intraplate events may be due to higher crustal strength and stresses far from active faults.

Stress drops may also be sensitive to the type of tectonic regime. For example in southern California, Shearer *et al.* (2006) identified higher-than-average stress drops in some regions containing a relatively high fraction of normal-faulting events whereas the mainly reverse-faulting aftershocks of the Northridge earthquake have lower-than-average stress drops. In contrast, the global study of Allmann & Shearer (2009) found higher-than-average stress drops for strike-slip events. Furthermore, stress drops are observed to be lower for regions of relatively high heat flow in Japan (Oth 2013) and increase with depth, for example, in southern California (Shearer *et al.* 2006; Yang & Hauksson 2011; Hauksson 2015) and Japan (Oth 2013). In addition to fault proximity, tectonic regime, heat flow and depth, stress drops have also been observed to vary as a function of recurrence intervals and loading rates in the laboratory and nature (e.g. Kanamori *et al.* 1993; He *et al.* 2003). Slower loading rates and longer healing periods within interseismic periods lead to an increase in asperity strengths and stress drops (Beeler *et al.* 2001).

In this study, we investigate regional stress-drop variations close to the San Andreas fault zone within the greater San Gorgonio Pass (SGP) region. Our analyses are based on newly available broadband seismic records. In contrast to earlier, large-scale studies, the present work provides a detailed discussion of regional seismotectonics and possible origins of stress-drop variations within a localized area. We expand on previous studies by including a systematic correlation between stress drops and geologic slip rates as well as lithological variations across the SGP region. The SGP region has received much attention because of its unknown role in hindering or supporting a large-magnitude through-going earthquake rupture on the southern San Andreas (e.g. Magistrale & Sanders 1996; Graves *et al.* 2008). This region also provides an ideal natural laboratory to study stress-drop variations because of its high seismic activity, station density and well-studied tectonics. We first review the tectonic setting (Section 2) and then introduce the method for estimating source spectra and stress drops largely following Shearer *et al.* (2006) (Section 3). We determine spatial variations in stress-drop estimates and assess their reliability (Sections 4.1 and 4.2). We then perform a detailed analysis of crustal parameters that may influence stress-drop variations (Sections 4.3–4.5). More details about the stress-drop computations can be found online in the Supporting Information.

2 SEISMIC DATA AND TECTONIC SETTING

2.1 Seismicity catalogues and waveform data

We analysed seismicity and source parameters close to SGP (Fig. 1), a region of high geometric complexity within the San Andreas fault system. The present study is based on three different types

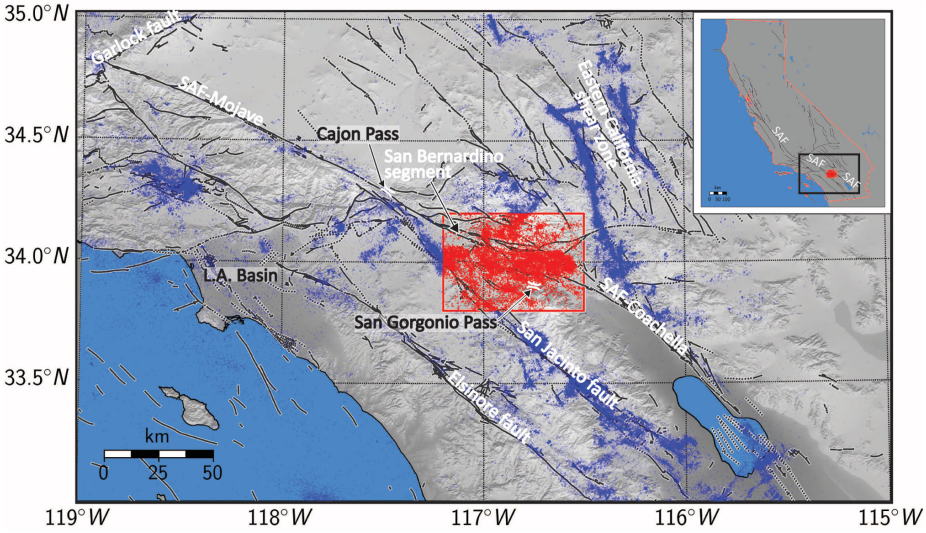

Figure 1. Overview of major faults (black) and seismicity within the study region (red markers). Background seismicity is shown in blue. The inset shows the map location with respect to the Californian state boundaries and the San Andreas fault (SAF).

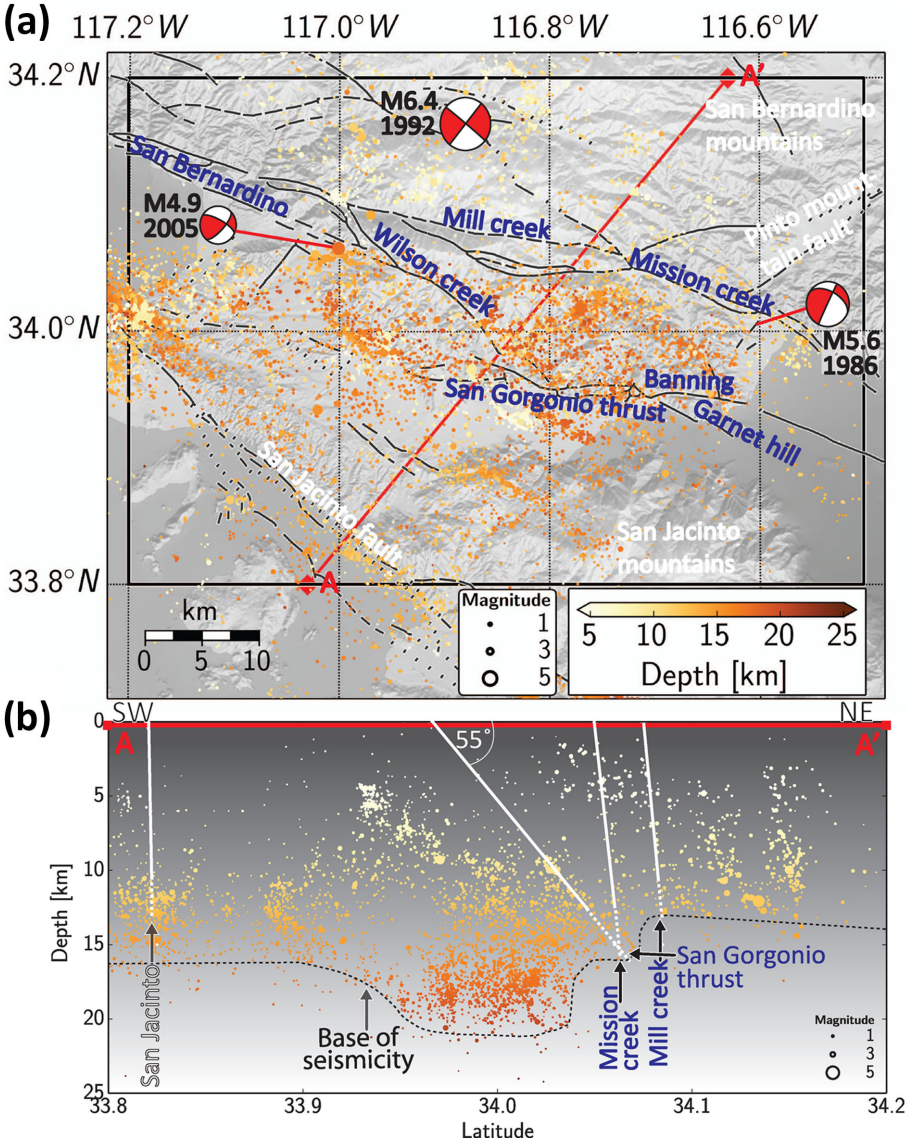

Figure 2. Seismicity within the SGP region in map view (a) and within a 2-km wide depth cross-section between A and A′ (b). Different fault segments that comprise the San Andreas fault system are labelled in blue. The beach balls in (a) mark the locations and focal mechanisms of the 1992 M_w6.4 Big Bear, the 1986 M_w5.6 North Palm Springs and the 2005 M_w4.9 Yucaipa earthquake. The fault orientations in (b) are constructed using mapped fault traces, approximate dip angles and near-by seismicity clusters. Seismic events are broadly distributed and can only partially be associated with mapped fault traces (e.g. for Banning and Mission Creek fault) highlighting the complexity of the deformation within the area.

of data: (1) a relocated earthquake catalogue that improved single event location by using a 3D velocity structure, source-specific station terms and relative traveltime differences from waveform cross-correlations of event clusters (Shearer *et al.* 2005; Hauksson *et al.* 2012); (2) focal mechanisms, estimated from first-motion polarities and amplitude ratios of *P* and *S* waves (Yang *et al.* 2012); (3) seismic waveforms, obtained from the Southern California Earthquake Center data centre, which we used to determine source spectra and source parameters. We limited our analysis to events that were recorded at broad-band stations. These stations show a largely consistent frequency response from ∼0.2 to 50 Hz with a sampling frequency of 100 Hz. This wide frequency band is beneficial for improving the resolution of corner frequency estimates and high-frequency fall-offs compared to previous studies. The broad-band data are available for a dense array of stations in southern California starting in ∼2000. We selected a period from 2000 to 2013 because of the availability of relatively homogeneous waveform records, station instrumentation and seismicity catalogues. During this period over ∼11 300 seismic events with magnitudes in the range of M_L = 0–4.88 occurred within the study region. The largest event occurred near the San Bernardino segment of the San Andreas fault in June 2005 (see Fig. 2).

2.2 Tectonic complexity within the SGP region

The study area is crosscut by several faults that comprise the San Andreas fault system. The San Andreas fault system is characterized by relative structural simplicity in the Coachella segment to the southeast and the Mojave segment to the northwest of SGP (Fig. 1). The SGP region, on the other hand, is marked by complex, distributed crustal deformation. Tectonic slip within this region is

accommodated by systems of strike-slip and thrust faults (Allen 1957). These fault segments include the Garnet Hill and Banning segments to the northwest of the Coachella segment, followed by the San Gorgonio thrust fault (SGF), Wilson Creek and San Bernardino segments and the Mill and Mission Creek segments north of SGP (Fig. 2). The Banning segment became less active about 5 Myr ago (e.g. Yule & Sieh 2003). Consequently, the slip on the San Andreas fault system may partially bypass the SGP region, for example, via the San Jacinto fault to the west (Allen 1957; Yule & Sieh 2003; Langenheim *et al.* 2005; McGill *et al.* 2013).

The San Andreas fault within the SGP region lacks continuity because the regional deformation is strongly influenced by a restraining step within the Mission Creek section (Fig. 2a). As a result, several secondary fault strands exist, which are oriented unfavourably with respect to the tectonic plate motion, leading to large-scale transpressional tectonics (Carena *et al.* 2004; Langenheim *et al.* 2005; Cooke & Dair 2011). This tectonic complexity is also articulated in the distribution of seismic events, which occur preferably off the main fault strands (e.g. Yule & Sieh 2003). Similarly, the tectonic complexity can be observed in the diversity of focal mechanism solutions which show predominant oblique, sinistral slip above 10 km. In contrast, below 10 km depth, oblique strike-slip, normal and thrust faulting accommodate east–west extension and north–south compression (Nicholson *et al.* 1986). The thrust faulting within the SGP region resulted in a high magnetic anomaly, likely caused by the wedging of Peninsular Range rocks underneath Transverse Range material and the presence of deep, magnetic rocks of San Bernardino or San Gabriel basement types (Langenheim *et al.* 2005). The convergence rates within this area are estimated at 1–11 mm yr^{-1} (Yule *et al.* 2001; Langenheim *et al.* 2005). The longterm fault slip rates decrease systematically when approaching the SGP region from the north and south from 24.5 ± 3.5 and 14–17 mm yr^{-1} respectively down to 5.7 ± 0.8 mm yr^{-1} (Dair & Cooke 2009; Cooke & Dair 2011; McGill *et al.* 2013). Since the 1940s, three main shocks above *M*4 have been recorded within the study area: (1) the 1986 M_w5.6 North Palm Springs, (2) the 1992 M_w6.4 Big Bear, and (3) the 2005 M_w4.9 Yucaipa earthquake (Fig. 2a). In addition, three larger earthquakes were recorded nearby, that is, the 1948 M_w6.0 Desert Hot Springs and 1992 M_w6.1 Joshua Tree earthquakes to the east as well as the 1992 M_w7.3 Landers earthquake to the northeast.

Seismicity becomes deeper north of the SGF, which dips at about $\sim 55^\circ$ underneath the San Bernardino mountains (Fig. 2b). The base of the seismicity beneath the San Jacinto mountains dips gently to the north (Fig. 2b). This is followed by an abrupt step in the seismicity base from ~21 to 13 km below the Mission Creek segment. This step marks the boundary between Peninsular and Transverse Range rocks (see also Nicholson *et al.* 1986; Yule & Sieh 2003). The corresponding influence on stress drops is discussed in Section 5.2.2. The depth profile of the relocated seismicity catalogue suggests that the seismicity step may be slightly disturbed by the presence of the SGF, leading to seismically active underthrusting of Peninsular Range rocks beneath the Transverse Ranges. Based on mapped surface traces and approximate fault dip angles (Fuis *et al.* 2012), we connected fault surface expression with seismicity clusters at seismogenic depth (Fig. 2). The SGF is approximately co-located with the transition between deep seismicity to the south and shallower seismicity to the north. Faults to the south generally lack seismicity above ~5 km whereas faults to the north (e.g. Mission and Mills Creek) produce seismic events from shallow depths down to 14–15 km.

3 METHOD: SOURCE SPECTRA INVERSIONS AND STRESS-DROP ESTIMATES

This study uses the method developed by Shearer *et al.* (2006), which has been described in many previous publications (e.g. Allmann & Shearer 2007, 2009) and is thus only briefly summarized here. Instead of modelling amplitude spectra individually for each event and station, we invert the entire data set for average event, path and station terms by stacking over common receivers, paths and events (Shearer *et al.* 2006). This stacking increases the stability and smoothness of estimated source spectra thereby also improving the robustness of spectral fits and source parameter estimates. The method involves four key analysis steps: (1) separation of recorded spectra into source, path and site spectra; (2) calibration of relative moment estimates to absolute seismic moments using local magnitudes; (3) correction of high-frequency attenuation using a regional empirical Green's function; (4) spectral fitting of corrected source spectra to obtain source parameters for each event. These steps are described briefly in the following sections.

3.1 Separation into source, path and site-response spectra

Amplitude spectra were computed for tapered waveforms within a 1.28 s time windows after *P*-wave arrivals and equal length windows before *P*-arrivals for noise spectra. This comparably short time window provides reliable results for our small-magnitude data set for which event-station distances are small and *S*-wave arrivals occur close to *P*-arrivals. For the spectral inversion, we required a signal-to-noise ratio (SNR) above 5 within three different frequency bands (5–10, 10–15 and 15–20 Hz) as well as at least five station picks per event. The recorded waveforms at each station are a convolution of source, path and site contributions, which changes to a multiplication in the frequency domain and to a summation in the log-frequency domain and can thus be expressed by the following system of linear equations:

$$d_{ij}(f) = e_i(f) + t_{ij}(f) + s_j(f), \quad (1)$$

where d_{ij} is the logarithm of the recorded amplitude spectrum, e_i and s_j are the event and station terms and t_{ij} is the traveltime term between the *i*th event and *j*th station (see also Fig. S1). This system of equations can be solved iteratively by estimating event, station and path terms as the average of the misfit to the observed spectra minus the other terms (e.g. Andrews 1986; Warren & Shearer 2000; Shearer *et al.* 2006; Yang *et al.* 2009). For robustness, we suppressed outliers by assigning L1 norm weights to large misfit residuals.

The path terms, t_{ij}, in eq. (1) were discretized at each iteration by binning at 1-s intervals according to the corresponding *P*-wave traveltimes. The stacked path terms capture the average, large-scale effects of geometric spreading and attenuation along the ray pay. These terms show systematic variations in spectral amplitudes which are in agreement with a theoretical attenuation model with $Q \approx 550$ (Fig. S3, online supplement). The source terms are discussed in detail in Section 3.3. The robustness of the spectral inversion method for large data sets was verified previously by a comparison with theoretical results and synthetic data (Shearer *et al.* 2006; Allmann & Shearer 2007).

We do not attempt to resolve take-off angle dependent differences in recorded spectra arising from radiation pattern and directivity effects, which are a potential source of uncertainty within the source spectra estimates (e.g. Kaneko & Shearer 2014). However, these

differences are reduced to some extent by stacking spectra from many stations and thus averaging over the focal sphere.

3.2 Calibration to absolute seismic moment

We estimated the relative seismic moment, Ω_0, for individual source spectra from the corresponding low-frequency contributions by averaging the spectral amplitudes from the first three data points above 1 Hz (see Table S1 for a summary of utilized frequency bands). We then calibrated the relative moments using the catalogue magnitudes, assuming that the low-frequency amplitudes are proportional to moment, and that the catalogue magnitude is equal to the moment magnitude at $M_L = 3$.

3.3 Source spectral stacks and high-frequency correction

We determined a common high-frequency correction term by stacking all source spectra within 0.2 magnitude bins. This term is similar to an Empirical Green's Function (EGF) used for co-located earthquakes and removes the ambiguity in the absolute spectral level. The EGF was determined by fitting a constant stress-drop, Brune-type spectral model (see following section) between 2 and 20 Hz to the magnitude-binned spectra. The EGF is then determined from the average misfit between theoretical and observed spectral shapes. The corrected, magnitude-binned spectra generally show shapes expected from a Brune-type model, that is, approximately constant values at long periods and f^{-2} fall-off at short periods (Fig. S2). Furthermore, correcting the mag-binned spectra for differences in seismic moments by shifting along a f^{-3} line results in a data collapse, indicating self-similar behaviour and constant stress drop at a large scale (Fig. S2). Our best-fitting, constant-stress-drop model with reasonable fit to the mag-binned spectra has a stress drop of 6.1 MPa. In the following, the regional EGF is used to correct average source terms of individual events to search for possible smaller scale variations in stress drops. We also experimented with stacking subsets of event spectra to determine spatially varying EGFs, however, no significant difference in the stress-drop estimates was observed within the comparably small study region in San Gorgonio.

3.4 Spectral model and stress-drop estimates

After correcting the source spectral estimates for the regional EGF, we fit individual event spectra with the f^{-2} model of Brune (1970) to obtain corner frequency estimates and then apply the Madariaga (1976) model to obtain stress-drop estimates. Here, we used a spectral model that has the following form (Brune 1970):

$$u(f) = \frac{\Omega_0}{1 + (f/f_c)^2} \tag{2}$$

where Ω_0 describe the low frequency plateau and f_c the corner frequency. The observed spectra were fitted using Ω_0-values determined according to Section 3.2 and using a grid-search algorithm to compute f_c. The grid search minimized the rms misfit between the log-transformed observed and theoretical spectra between 2 and 20 Hz.

For a circular, isotropic rupture and constant rupture velocity, the stress drop ($\Delta\sigma$) and P-wave corner frequency can be related by (Eshelby 1957; Madariaga 1976)

$$\Delta\sigma = M_0 \left(\frac{f_c}{0.42\beta} \right)^3, \tag{3}$$

where M_0 is the seismic moment and β is the shear wave velocity.

The bandwidth for spectral fitting using eq. (2) is limited to 2–20 Hz, but corner frequencies can be estimated up to larger values if the Brune model is exactly correct, such that the small differences in spectral fall-off below 20 Hz are reliable predictors of behaviour at higher frequencies. Because individual spectra, even when stacked over many stations, are more irregular than the Brune model, our corner frequency estimates become increasingly uncertain at higher frequencies, corresponding to our largest stress-drop estimates. In these cases, we can say with some confidence that the stress drops are higher than average but we have less confidence regarding their exact values and the determined f_c values may primarily present lower bounds of the true corner frequency. We chose to include these values to obtain as complete as possible spatial sampling of stress-drop variations without biasing the results by introducing arbitrary cut-offs. This is especially important to avoid biases caused by excluding, for example, high corner frequency earthquakes, which can result in artificially reducing stress-drop variations.

Similar to other large-scale stress-drop studies (e.g. Shearer *et al.* 2006; Allmann & Shearer 2007), our observations show large differences in stress-drop estimates even among nearby events, however, by averaging results from many events, robust spatial variations in stress drops can nonetheless be identified. Our method enables us to analyse large seismic data sets in a uniform fashion to obtain estimates of source parameter variations as reliably and consistently as possible. However, the scatter in stress-drop estimates is expected to be large as a consequence of uncertainties in corner frequency, limited station coverage as well as variations in rupture geometry and velocity. In the results that follow, we experiment both with assuming a constant reference shear velocity, β, of 3.5 km s^{-1} and allowing β to increase with depth (see Section 4.3).

It is also important to recognize that different models, such as those of Brune (1970), Sato & Hirasawa (1973), Madariaga (1976) and Kaneko & Shearer (2014), will yield differences in absolute stress-drop values that vary by up to a factor of five, even when the same rupture velocity is assumed. Here we use the Madariaga (1976) model for consistency with our prior work and thus our results should only be directly compared with other studies that also assume the Madariaga (1976) model. That is, the absolute values of our stress-drop estimates are not well-constrained because they are model and rupture velocity dependent. However, relative variations in our estimated stress drops are better constrained and are indicative of fundamental source properties. Our high-stress-drop events have higher corner frequencies and radiate more high-frequency energy than low-stress-drop events of the same size. Characteristic variations in high-frequency contributions of source-spectral radiation are shown in Fig. S4 for events with similar relative moments.

4 RESULTS

Here we describe lateral variations in mean stress drops and explore possible underlying differences in crustal conditions. Mean values refer to the mean of the underlying lognormal distributions (Andrews 1986), which are approximately equal to the median but deviate substantially from the Gaussian-mean due to the left-skewness of lognormal distributions (see Fig. S6). In addition to the lognormal mean, we also report standard deviations and statistical significance of variations of underlying distributions (see also Fig. S11 and Table S1).

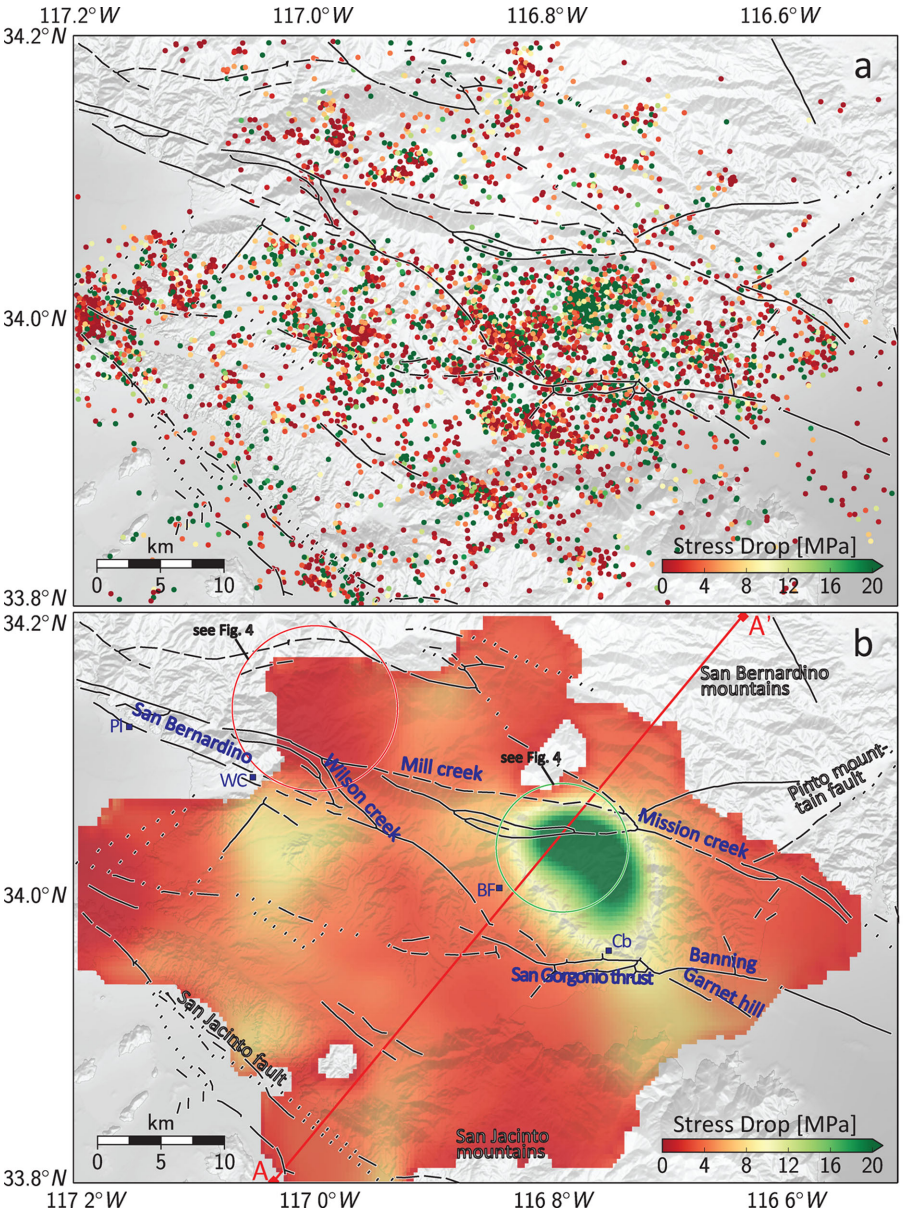

Figure 3. Map view of individual event (a) and smoothed (b) stress-drop estimates within the study region. Fault segments of the San Andreas fault system are labelled in blue. The red line from A to A′ marks the location of the depth cross-sections in Figs 2(b) and 8. The blue squares show the sites of geologic slip rate estimates (see Fig. 10 and description for details). Stress drops vary substantially from about 1 MPa to more than 20 MPa (see the colour bar).

4.1 Spatial variations in estimated stress drops

Fig. 3(a) shows our individual event stress-drop estimates (assuming a fixed rupture velocity) for the study region, which vary from about 0.3 to 100 MPa, with a mean value of about 5 MPa. Despite the scatter, regions of higher and lower mean stress drop can be identified, such as the lower stress-drop region close to [−117.2, 34] and the higher stress-drop region close to [−116.78, 34]. To better assess the spatial variations of mean earthquake stress drops, we smooth the results using a spatial median filter for the closest 60 epicentres to a 2-D uniform grid within a maximum area of $r = 5$ km (Fig. 3b). The maximum kernel width is chosen to avoid associating mean stress drops with too distant events. The resulting variations in mean stress-drop range from ∼2 to 20 MPa. The most striking feature in Fig. 3(b) is the region of anomalously high stress drops between the SGF and Mill Creek fault traces. Within this area, mean stress drops change rapidly (from north to south along longitude = 116.8°W) from ∼5 MPa up to >20 MPa and back to <5 MPa. In addition, we observe several regions of increased stress-drop estimates, for example, located close to the San Jacinto fault [−117.08, 33.9] and south of the San Bernardino segment [−117.05 34.07]. The dark red to orange regions highlight areas with stress drops between 2 and 8 MPa (see legend in Fig. 3).

Before probing different crustal parameters that could explain the observed variations in stress-drop estimates, we tested the robustness of the observed variations in stress-drop estimates. We started by investigating the difference between the high- and low-stress-drop regions (green and red circles in Fig. 3) focusing on the relation between corner frequencies and moment. We created a subset of data containing events within the two regions and performed a separate inversion for source spectra and source parameters. This inversion incorporates local EGF estimates which can account for smaller-scale variations in the attenuation structures. Systematic

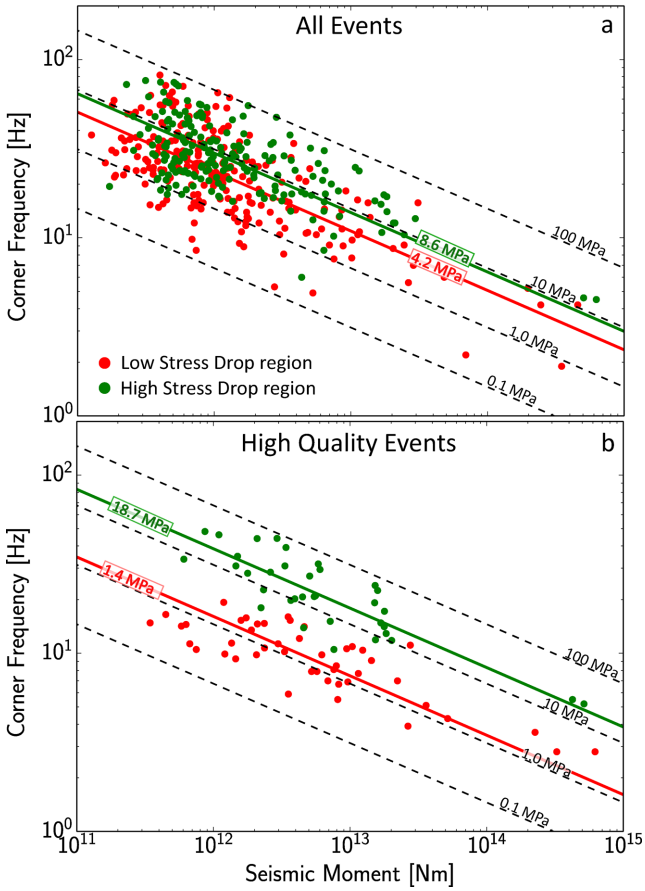

Figure 4. Corner frequency and seismic moment for events within a high (green circle in Fig. 3) and a low stress-drop regions (red circle in Fig. 3), for all events (a), and only high quality events, that is, events with an SNR≥10 that were recorded at more than 15 stations. The black, dashed lines highlight constant stress drops from 0.1 to 100 MPa and the green and red lines mark the mean stress drops (assuming lognormal-distributed data) for the two different regions. The variations in both (a) and (b) are statistically significant at the 99 per cent level.

variations in stress drops should lead to a separation between M_0 and f_c along lines of constant stress drops (Fig. 4). Our tests approximately confirmed this expectation in that average corner frequencies are higher for the high-stress-drop regions compared to the low-stress-drop regions. However, we also observed significant scatter in Fig. 4(a) especially for the smaller events with low seismic moments. To estimate how much of this scatter is due to measurement uncertainties and how much can be attributed to underlying physical processes, we determined M_0, and f_c for high-quality records only, that is, records with SNR $\geq$ 10 and at least 14 contributing stations (Fig. 4b). The corresponding statistically significant variation in mean stress drops between $\Delta\sigma$ = 1.4 and 18.7 MPa suggests that our method can resolve lateral variations in stress drops above the measurement uncertainties. These values are comparable to the values for the same regions in Fig. 3. Moreover, restricting the analysis to the highest-quality source spectra estimates resulted in a reduction of scatter and a clearer separation of low- and high-stress-drop regions partially due to excluding most of the smallest-magnitude events. A more detailed investigation of the dependence on stress drops on input parameters in source-spectral inversions and data selection can be found in the Supporting Information (e.g. Figs S6–S9).

Following the analysis of corner frequency and moment, we compared the relative frequency content of seismic event waveforms within the low- and high-stress-drop regions. To this aim, we juxtaposed low- and high-stress-drop source spectra after normalizing spectral amplitudes by moment and frequencies by the corner frequency derived from eq. (3) based on the regional mean stress drop (Fig. 5). The normalization resulted in a shift of the original frequency band to lower frequencies, which is most pronounced for events with small seismic moments. This re-scaling corrects for differences in moment within the individual regions but also shows the differences in frequency content of individual events, thus providing a qualitative estimate of variations in corner frequency. In case of constant stress drop, the shifted source spectra should collapse onto the same curve. However, as expected the present data subsets display strong variations within the two different regions: Low-stress-drop events have lower corner frequencies and plot further to the left (Fig. 5a), whereas high-stress-drop events exhibit relatively higher corner frequencies and plot further to the right (Fig. 5b). Consequently, the relative difference between spectra within the low- and high-stress-drop regions further supports the reliability of observed spatial variations in stress drops.

4.2 Sensitivity analysis of stress-drop computations

To investigate the dependence of source inversion results on input parameters, we conducted a sensitivity analysis of selection criteria for the input spectra. The details of the sensitivity analysis can be found in the Supporting Information. Generally, the analysis confirmed the statically significant differences between low- and

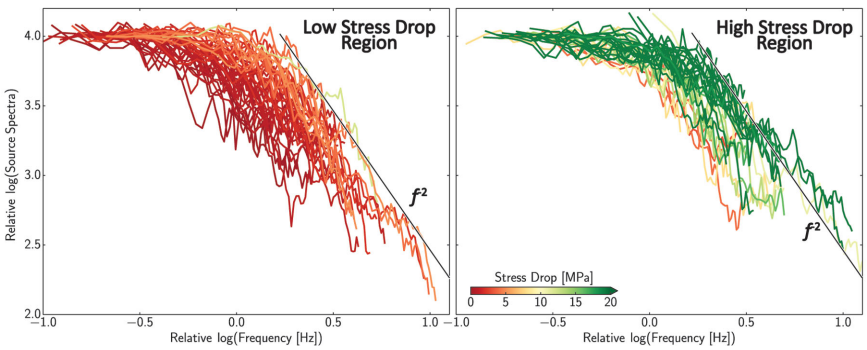

Figure 5. Source spectra for events within an area of low (left) and high (right) stress drop corrected for differences in moment by shifting along f^{-3} and coloured according to stress drop. The solid, black line highlights a high-frequency fall-off slope of −2. High-stress-drop spectra are generally shifted further to the right due to higher corner frequencies and a smaller proportion of low-frequency contributions compared to the area of low stress drop.

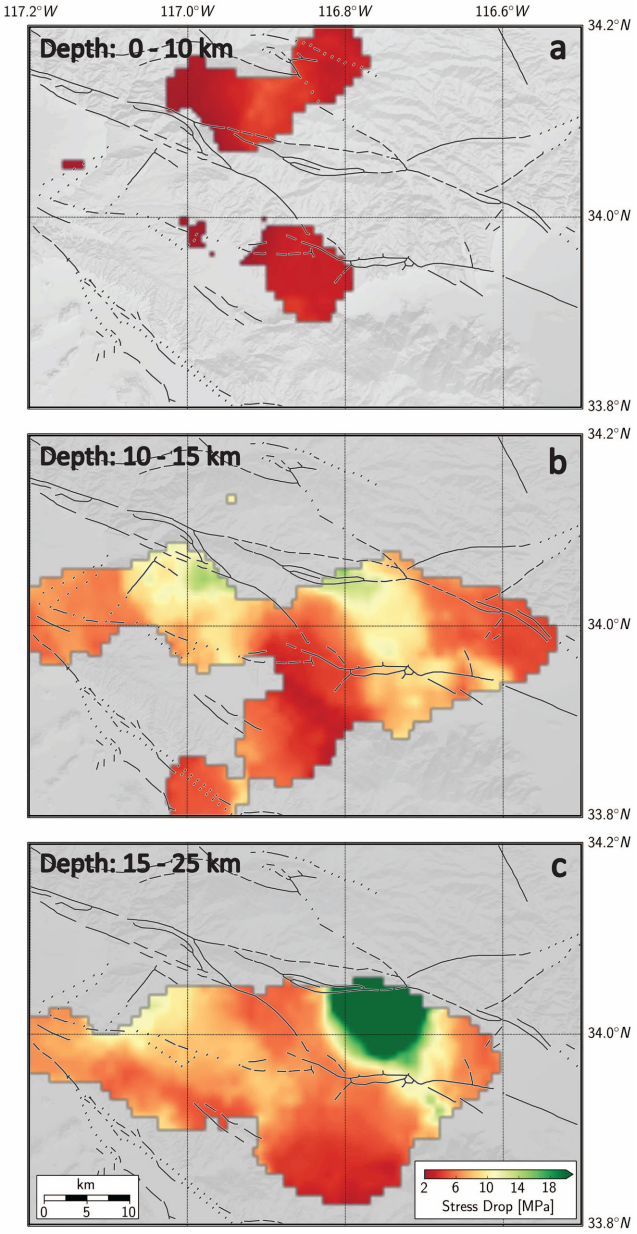

Figure 6. Smoothed spatial variations in stress drop for events within three different depth layers from 0–10, 10–15 and 15–25 km.

high-stress drop regions but also showed that the absolute stress drops may vary as a function of input parameters and data selection criteria. Limiting the analysis to records with many station picks had a larger influence on stress drops then choosing only high SNR records. Though absolute values may vary, the sensitivity analysis demonstrated that relative variations in stress drops can be identified reliably if the input parameters are chosen consistently.

4.3 Stress-drop variations with focal depth

To test the influence of focal depths and to examine possible lateral variations as a function of depth, we constructed smoothed stress-drop maps for three different depth ranges (Fig. 6). Because there are only few events above 5 km depth, we chose the first depth layer from 0 to 10 km, the second from 10 to 15 km and the third for events from 15 to 25 km. We observed a systematic difference in stress-drop estimates between the depth layers. The shallow events (0–10 km) were dominated by low stress drops, the intermediate depth layer includes some of the high stress drops and the deepest events clearly highlight the area of anomalously high stress drops between the San Gorgonio and Mission Creek fault traces. As expected, the intermediate and the bottom depth layers do not include the low-stress-drop region towards the northern edge of the study region, which was dominated by relatively shallow events (see Fig. 2b).

Motivated by the observation of stress-drop variations for different depth layers, we probed for a general correlation between focal depths and stress drops. Stress drops for events shallower than 10 km are low, with mean values from 2.6 to 3.0 MPa. At ∼10 km the mean stress drops increase abruptly to ∼4.8 MPa. At depths from ∼10 to 17 km, mean stress drops continue to increase gradually up to ∼5.5 MPa before decreasing to 5.3 MPa at 20 km depth. This shows that deep earthquakes in our study region have higher average corner frequencies and radiate more high-frequency energy than shallow earthquakes.

However, because our results described so far assume a constant rupture velocity for all events, at least some of the apparent increase of stress drop with depth could be explained as an increase in rupture velocity with depth. To test for this possibility, we repeated our stress-drop calculations under the assumption that the rupture velocity is proportional to shear velocity variations with depth. We used a regional velocity model (Langenheim *et al.* 2005), which has a high velocity anomaly just beneath the SGP region. We corrected our initial stress-drop estimates using two different depth profiles that capture the average seismic velocity changes beneath and outside of the SGP region, including a relatively high velocity zone at about 7–13 km depth (Fig. 7b). The results are shown by the round markers in Fig. 7(a). Including a depth-dependent change in rupture velocity affected the variations in stress drops only marginally. This is expected because most of the variations in seismic velocities are located close to the surface from 0 to 6 km whereas the largest changes in stress drops are at greater depths. The rupture velocity (V_r) would have to change abruptly by a factor of 1.2 near 10 km to compensate the observed increase in stress drop with depth, but the inferred increase in V_r at this depth is only about 3 per cent.

The analysis of stress-drop variations with depth revealed larger values for relatively deep events (below 10 km). To put this finding into the seismo-tectonic context of the SGP region, we mapped stress drops of individual events along the depth cross-section highlighted in Fig. 3. The previous results of lower stress drops above 10 km are supported by the overall stress-drop distribution (Fig. 8a). However, we also observed a relatively dense cluster of high-stress-drop events in immediate proximity to the seismicity step extending from the base of the seismicity up to the SGF. This region marks the location of the deepest earthquakes within the study area. The transition to the hanging wall of the SGF is characterized by a notable decrease in stress drops. Similarly stress drops decrease to the southwest at greater distances to the seismicity step.

The position of the seismicity step itself is likely connected to relatively strong transpressional tectonics, which can be derived from the motion along the SGF and predominant thrust-type focal mechanisms within the same region (Fig. 8b). Although there is an apparent dominance of underthrusting within this area, we also observed normal and strike-slip events throughout the depth cross-section. In the following, we investigate possible systematic correlation between dominant faulting mechanisms and stress drops.

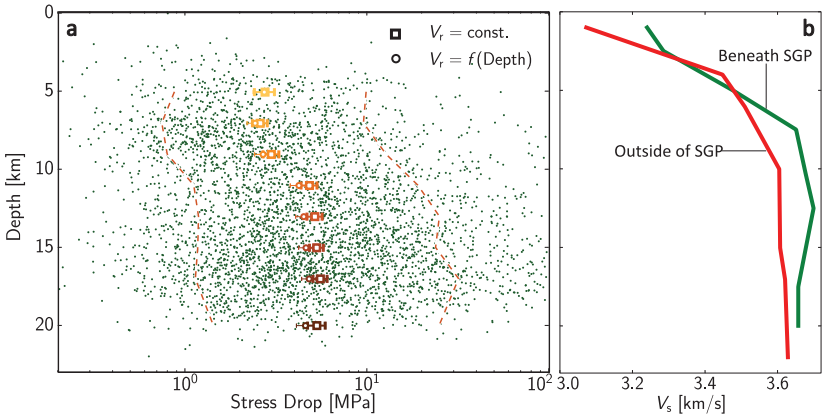

Figure 7. Variations in stress drops as function of depth (a). Green dots show individual event stress drops and squares show the binned, mean stress drops with 2σ uncertainties estimated from bootstrap resampling (horizontal error bars). Circles display stress drops after correcting for a depth-dependent rupture velocity using two different 1-D velocity profiles (b) for events beneath (green curve) and outside (red curve) of SGP. The dashed lines in (a) show 10th and 90th percentiles.

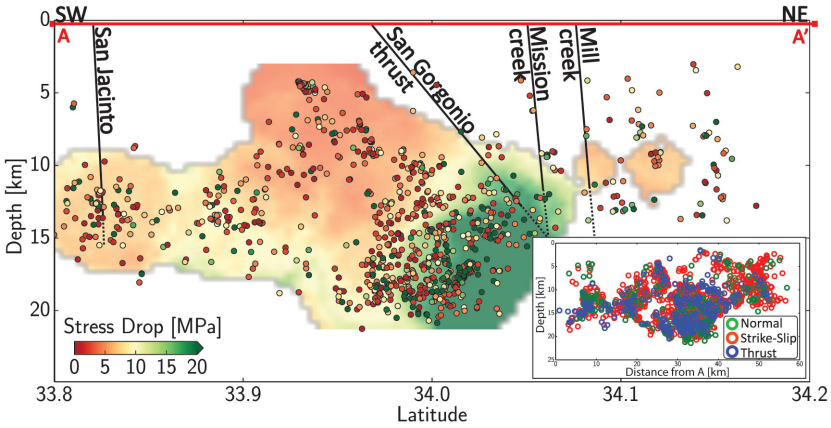

Figure 8. Same depth cross-section as in Fig. 2 bottom, now with events coloured and scaled according to stress drop. The background colours depict the spatial distribution of mean stress drop, smoothed as in Fig. 3. The deep events southwest of the Mission Creek segment are connected to clusters of locally high stress drops whereas events above 10 km seem to be marked by generally shallow stress drops. Inset: focal mechanism solutions for events along profile A–A′ in Fig. 8 strike-slip mechanisms in red, thrust in blue and normal faulting in green.

4.4 Stress-drop variations as function of faulting mechanism

We correlated average faulting mechanisms expressed by their differences in rake angle (Fig. 9). These differences can be quantified by normalizing the observed rake angles so that the spectrum of faulting mechanisms can be expressed on a continuous scale from -1 to 1 with normal faulting at -1, strike-slip at 0 and thrust faulting at a value of 1 (Shearer *et al.* 2006). Stress drops and focal mechanisms show a weak, positive correlation so that normal faulting has relatively lower mean stress drops ($\Delta\sigma = 3.9 \pm 0.7$ MPa) whereas thrust faulting has higher mean stress drops ($\Delta\sigma = 6.0 \pm 1.7$ MPa). Differences in lognormal means as a function of focal mechanisms are only statistically significant between normal and strike-slip events. Strike-slip events represent the predominant type of faulting. Consequently, their mean value ($\Delta\sigma = 5.3 \pm 0.5$ MPa) is similar to the one observed for the whole region.

4.5 Stress-drop variations along the San Andreas fault system

One of the fundamental questions concerning the SGP region is the possibility of large ruptures that could propagate through the entire region, for example, from Cajon Pass to the Salton Sea (Graves *et al.* 2008). Using the average fault orientation within the Mojave segment (see Fig. 1), we determined variations in stress-drop estimates in the proximity of a possible path of such a rupture between the San Bernardino and Garnet Hill segments (Fig. 10). The stress drops decrease to the southeast of SGP within the area of the Banning and Garnet Hill segments that eventually merge with the Coachella segment of the San Andreas fault. The stress drops also decrease to the northwest of SGP and show consistently lower values outside of the SGF segment.

The stress drop traverse through the SGP is located in immediate proximity to local slip rate estimates along the SAF (highlighted by blue squares in Fig. 3). Geologic slip rates were previously compiled from many different studies and summarized by Dair & Cooke (2009); Cooke & Dair (2011) as well as by McGill *et al.* (2013) highlighting a systematic decrease from Cajon Creek (slip rates $= 24.5 \pm 3.5$ mm yr^{-1}) to Cabezon (5.7 ± 0.8 mm yr^{-1}), which is close to SGP. To the southeast, the slip rates increase again within the Coachella region (14–17 mm yr^{-1}) of the San Andreas fault. The average geologic slip rate on the SGF itself is estimated to be as low as 1.0–1.3 mm yr^{-1} (Matti *et al.* 1992). Stress-drop estimates show a statistically significant increase from ~3 to 10 MPa before decreasing again southeast of SGP. This shows that stress drop and

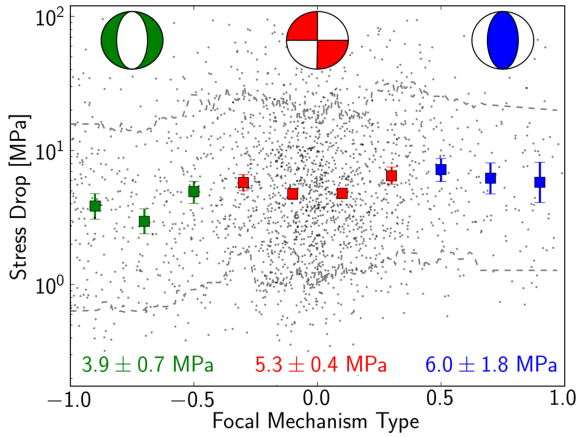

Figure 9. Variations in mean stress drop as function of faulting mechanism. The grey dots represent individual event stress drops and coloured, square markers show the binned lognormal means. Error bars represent the 95 per cent confidence limits of the mean determined by bootstrap resampling. Mean values for normal (green), strike-slip (red) and thrust (blue) faulting are shown at the bottom of the figure. Normal faulting is generally connected to relatively lower stress drops of ∼4 MPa whereas thrust faulting exhibits higher stress drops of ∼6 MPa.

slip rate estimates are approximately inversely correlated along the profile of the San Andreas fault zone. The stress-drop estimates are, in contrast to slip rate estimates, based on small-magnitude events that occur off the major fault segments. This may imply that low slip rates along major faults are also representative for many, adjacent secondary faults.

5 DISCUSSION

5.1 Seismicity and stress-drop variations

The most prominent feature in the seismicity is a lack of shallow events south of the Mission and Mill Creek segment and a seismicity step close to the down-dip end of the SGF. To the north, we observed more shallow seismicity that extends down to about 14–15 km depth. The latter conforms to the commonly observed depth extent of the seismogenic zone within southern California (Nazareth & Hauksson 2004). The variations in the maximum depth of seismicity may be related to both topographic and lithologic effects, supported by the sharpness of the transition and the approximate, inverse relationship between surface relief and seismicity base depth (Magistrale & Sanders 1996; Yule & Sieh 2003). The juxtaposition of different lithology caused by the large displacement along the San Andreas fault system seems to contribute to the creation of the observed difference in the maximum focal depths, moving the brittle-ductile transition to greater depths. The latter may be caused by a difference in plasticity temperature between feldspar-dominated Peninsular Range and quartz-dominated Transverse Range rocks (e.g. Scholz 1988; Magistrale & Sanders 1996). In addition, downthrusting along the SGF may perturb the geotherm downwards which can explain the locally deep earthquakes and base of seismicity. We explore this question in more detail below within the context of the observed changes in stress drops.

Stress drops within the present study show regional variations between ∼1 and ∼20 MPa. Similar variations are observed in laboratory earthquake-analogue experiments and seismicity at shallow depth in mines. The latter exhibited relatively high displacements and locally high stress drops of up to 70 MPa (McGarr *et al.* 1979). Shear stress drops during laboratory stick-slip experiments range from ∼1 to more than 160 MPa (e.g. Thompson *et al.* 2005; Goebel *et al.* 2012). The laboratory studies also highlight a connection between fault heterogeneity, aftershock duration and stress-drop magnitudes so that stress release is higher and aftershock duration shorter for smooth, homogeneous faults in the laboratory (e.g. Goebel *et al.* 2013a,b).

The here observed spatial variations in stress-drop estimates are similar to results by Shearer *et al.* (2006). The previous study applied the same approach to seismic records between 1989 and 2001, finding relatively high average values, similar spatial variability and an area of high stress drops between the San Gorgonio

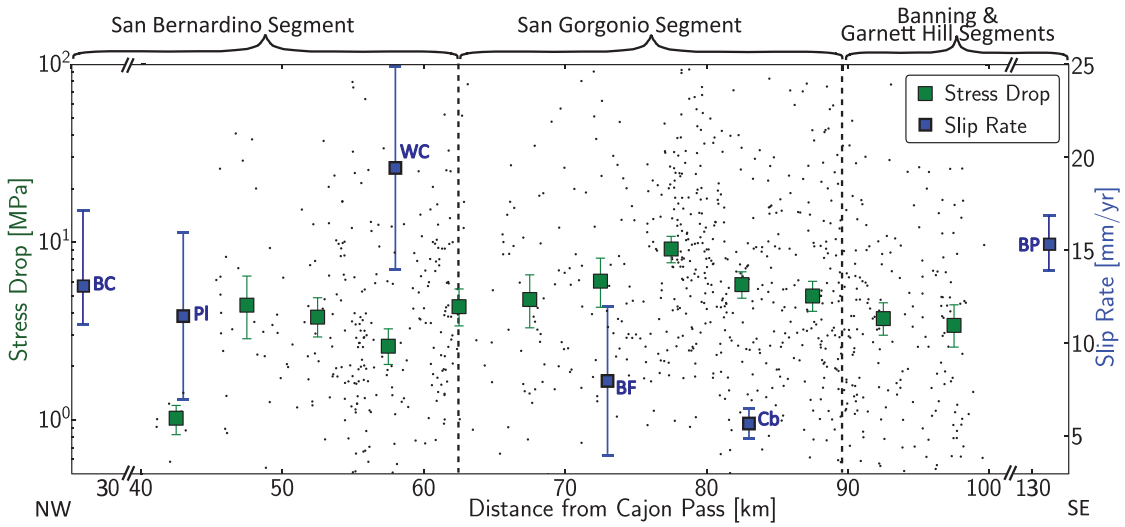

Figure 10. Changes in stress drop across the SGP region, that is, within a ∼10-km wide area around the San Andreas fault zone from NW to SE. The *x*-axis displays the distance along the San Andreas from Cajon pass (see Fig. 1 for Cajon pass location). Individual event stress drops are marked by grey dots and distance-binned, mean values by green squares. The 95 per cent confidence bounds of the mean, estimated by bootstrap resampling, are highlighted by green error bars. Geologic slip rates and uncertainties along the transect are highlighted by blue squares and blue error bars (see also Fig. 3 for the locations of slip rate estimates). The variation in mean stress drops with slip rates, for example, between Pl ($\Delta\sigma$ = 1–3 MPa) and BF ($\Delta\sigma$ = 7–8 MPa) is statically significant at the 99 per cent level. Sites of geologic slip rate estimates: BC: Badger Canon (McGill *et al.* 2013), Pl: Plunge Creek (McGill *et al.* 2013), WC: Wilson Creek (Weldon & Sieh 1985), BF: Burro flats (Orozco & Yule 2003), Cb: Cabezon (Yule *et al.* 2001), BP: Biskra Palms (Behr *et al.* 2010).

thrust and Mission creek fault. Given the nearly independent data sets, the agreement between the current study and Shearer *et al.* (2006) indicates that spatial-stress-drop variations are robust and approximately stable over time. The scatter in stress-drop estimates is slightly reduced in the present study, which is likely a result of the increased number of broad-band stations after 2001.

5.2 Measurement uncertainty versus physical variations in stress-drop estimates

Stress-drop estimates of small-magnitude earthquakes generally show large data scatter and it remained unclear from previous studies if this scatter is solely caused by multiple sources of uncertainty or if part of this variation has underlying physical causes. To address this question, we studied relative stress-drop variations and performed detailed tests of their robustness. This was accomplished by varying input parameters of the source inversion, investigating M_0-f_c ratios for different areas and by comparing individual source spectra themselves. Our tests revealed that a significant fraction of the stress-drop variations for small-magnitude earthquakes is rooted in physical differences in underlying rupture processes resulting in variable amount of high-frequency energy radiation for earthquakes with similar seismic moments (see, e.g. Fig. 5). We investigated a range of plausible crustal parameters that may influence stress drops in the SGP region.

5.2.1 Influence of focal mechanism types and ambient stress level

Differences in focal mechanism types are a proxy for larger compressive stresses and higher ambient stress level and may thus also influence the mean stress drops within a particular area. Previous investigations suggested a range of results, i.e., higher stress drops for both normal (Shearer *et al.* 2006), and strike-slip events (Allmann & Shearer 2009) while other studies reported no dependence on focal mechanisms (e.g. Oth 2013). Our results, on the other hand, suggest slightly higher stress drops for thrust events compared to strike-slip and normal faulting, however, not all of these variations are statistically significant at the 99 per cent level. The southern Californian data set was strongly influenced by the 1994 Northridge sequence which showed predominant thrust-type events with low stress drops (Shearer *et al.* 2006). A possible reason for the difference between our results and other studies may be related to the observational scales and the mixture of vastly different tectonic regimes. While our study concentrated on a small crustal region, others investigated stress drops for all of southern California (Shearer *et al.* 2006), Japan (Oth 2013) and a global data set Allmann & Shearer (2009), inevitably mixing seismic events from volcanic activity, off-shore events, induced seismicity and other sources. Over these large scales, stress level and faulting mechanics are bound to vary substantially, which may contribute more extensively to variations in stress drops than the differences in faulting mechanisms. Consequently, the rather weak correlation between focal mechanisms and stress drops as determined in the present study may indicate that the type of faulting is not the pre-dominant influence on stress-drops variations.

5.2.2 Influence of lithologic variations

The large cumulative displacement along the San Andreas fault system results in a juxtaposition of different lithology in many areas. Within the SGP area, feldspar-dominated Peninsular Range rocks have been moved next to quartz-rich Transverse Range rocks (Magistrale & Sanders 1996) with very different brittle-ductile transition temperatures (e.g. Scholz 1988). The difference in lithology and transition temperatures across the San Andreas fault system (or more precisely across the Mission Creek segment of the San Andreas fault) not only controls the thickness of the seismogenic zone but also influences the stress drops within the SGP region. The stress drops change abruptly across the Mission Creek segment so that feldspar-dominated rocks to the south accommodate substantially larger stress drops compared to quartz-rich material to the north of the Mission Creek segment. Similar observations have been made for mining-induced seismicity for which stress drops are higher in feldspar-dominated diorite dikes compared to the surrounding quartzite host rocks (Kwiatek *et al.* 2011). Kwiatek *et al.* observed a maximum difference in stress-drop estimates of about one order of magnitude whereas seismic velocities varied by only ∼3 per cent. Differences in ductility as a function of temperature also influence frictional properties, specifically, frictional strengths and slip stability (e.g. Tse & Rice 1986; Blanpied *et al.* 1995). Furthermore, the frictional stability, that is the degree of velocity strengthening or weakening of material interfaces, is directly connected to stress drop (e.g. Gu & Wong 1991; He *et al.* 2003; Rubin & Ampuero 2005). As a consequence, more ductile material, which favours velocity strengthening behaviour, also exhibits relatively lower stress drops compared to more brittle material. This behaviour has been measured not only for rocks at varying temperatures (e.g. Blanpied *et al.* 1995), but also, as in our case, for different rock types (quartz- versus feldspar-dominated) with different brittle/ductile transition temperatures.

5.2.3 Influence of asperity strengths and fault slip rates

The present study revealed an approximate inverse relationship between geologically inferred fault slip rates and stress drops so that the areas of highest stress drops are approximately co-located with the lowest slip rates (see Fig. 10). This is most pronounced for the largely locked SGP segment that also exhibits the highest stress drops. It should be noted that much of the seismicity in SGP occurs off the major fault traces for which geologic slip rates are known. Assuming that secondary faults in the proximity to the major fault segments have similar slip rates, we can explore a possible explanation for the correlation between slip rates and stress drops, which has also been observed in several previous studies. For example, long recurrence intervals and relatively high stress drops have been observed for large-magnitude earthquakes (M_w5.5–8.5; Kanamori 1986). In addition, small-scale laboratory experiments revealed a connection between loading rates, recurrence intervals and stress drops. In the laboratory, recurrence intervals of stick-slip events are correlated with fault strengths and stress drops so that longer recurrence intervals due to slower loading rates results in relatively high stress drops (Beeler *et al.* 2001). Similar results have been obtained for repeating earthquakes which show a higher proportion of high frequency energy radiation if the recurrence intervals between events are long (e.g. Beeler *et al.* 2001; McLaskey *et al.* 2012). The connection between earthquake recurrence and stress drops can be explained by increasing strength of load bearing asperities as a function of time. Asperities on a slowly loaded fault undergo relatively longer interseismic healing periods and exhibit higher resistance to shear before failure events occur, releasing a comparably high amount of stored stress. The amount of fault healing is, in addition to loading rates, also sensitive to pressure and temperature

conditions at depth, which can significantly influence the distribution of radiated seismic energy as a function of frequency (McLaskey *et al.* 2012). Increased asperity strength due to longer healing periods may also influence the tendency of asperities to fail individually. For instance, ruptures on heterogeneous faults with strong asperities are more likely to be arrested before growing to large sizes (Sammonds & Ohnaka 1998). The presence of strong asperities and fault heterogeneity may explain the relatively high stress drops of small- and intermediate-magnitude events that were observed here.

Theoretical considerations of seismic slip on a fault that is governed by rate-and-state friction confirm the dependence of stress drops on loading rates. In addition, the static stress drop ($\Delta\tau_s$) is sensitive to friction-parameters (e.g. Gu & Wong 1991; He *et al.* 2003; Rubin & Ampuero 2005):

$$\Delta\tau_s = \sigma_n(b-a)\ln(V_{dyn}/V_l), \tag{4}$$

where σ_n is the normal stress, b and a are material parameters that control the frictional behaviour, and V_l and V_{dyn} are the loading and dynamic slip velocities. The latter occupies values close to 1 m s^{-1}. Furthermore, if we assume approximately constant friction and normal stress along a fault segment, the stress drop changes as a function of loading velocity, V_l, so that a decrease in loading rate by a factor of 4–5, as observed in our study, corresponds to an increase in stress drop by factor of ∼1.7. Our results suggest an increase in stress drop along the San Andreas fault by a factor of 2–3 (see Fig. 10), which is slightly higher than predicted from this simple model. This difference can be explained by possible changes in material and frictional properties.

Spatial and temporal heterogeneity in stress drops may also be a result of variations in seismic coupling and transient slip processes before main shocks, for example, expressed by differences in foreshock and aftershock source spectra in southern California (Chen & Shearer 2013). Moreover, the SGP region is characterized by faults with large geometrical complexity. Ruptures on such complex faults may produce damage-related, seismic radiation that can increase the high-frequency content of source spectra so that stress drops appear higher (Ben-Zion & Ampuero 2009; Castro & Ben-Zion 2013).

In summary, we identified four parameters that potentially influenced stress-drop variations within the SGP region, that is, the type of faulting, hypocentral depths, geologic slip rates and mineralogical composition of the regional rock types. Our analysis suggests that all four mechanisms may to some degree contribute to stress-drop variations, however, focal mechanism types seem to play a minor role. The largest variations in stress drops occurred along the SAF-strike and in the proximity of the seismicity step at the down-dip end of the SGF. This suggests that average slip rates and the presence of abrupt lithologic changes exert the strongest control on stress drops. We hypothesize that relatively slow downthrusting of feldspar-dominated material in connection with longer healing periods and increased asperity strengths promote high stress drops both on the SAF and the adjacent secondary faults that produced much of the seismicity within the study region.

5.3 Implications for seismic hazard and earthquake rupture dynamics

The relatively high estimated stress drops and slow geologic slip rates within the SGP area suggest locally increased fault strength and long recurrence intervals. We hypothesize that areas of high stress drop are connected to the failure of individual small but strong fault patches. These strong asperities have a larger potential to fail individually as opposed to being linked-together in a large rupture, explaining the relatively high overall seismic activity but lack of $M > 5$ events within the study area. Consequently, rupture propagation may be hindered within the SGP area decreasing the probability of large earthquakes that propagate from the Salton Sea to Cajon Pass. The role of the SGP in hindering rupture propagation has been recognized previously based on the strongly segmented fault geometry within the area (Magistrale & Sanders 1996). The slip along the San Andreas fault system may increasingly by-ass the SGP region to the north and southeast, for example, via the San Jacinto fault (McGill *et al.* 2013).

6 CONCLUSION

We have analysed the spatial variation in source parameters of small- and intermediate-magnitude earthquakes within the SGP region. Our analysis revealed earthquakes with relatively high stress drops between the surface traces of the San Gorgonio thrust and the Mission fault. Furthermore, stress drops increase abruptly below ∼10 km depth and at the interface between Peninsular and Transverse Ranges. The latter is likely related to differences in lithology between the two geological formations so that feldspar-dominated Peninsular Range material favours relatively larger stress drops whereas quartz-dominated Transverse Range rocks exhibit relatively lower stress drops. Stress-drop estimates are approximately inversely correlated with longterm slip rates along the San Andreas fault system so that rapidly loaded fault zones are connected to lower stress drops whereas slow-slipping faults create events with higher stress drops. While several factors may contribute to stress-drop variations, our results suggest that within the greater San Gorgonio area, variations in rate of tectonic deformation and lithology are the predominant mechanisms. Understanding underlying mechanisms of stress-drop variations is essential to better constrain rupture propagation of major earthquakes and associated regional seismic hazards.

ACKNOWLEDGEMENTS

We thank Yehuda Ben-Zion and Adrien Oth for detailed reviews of an earlier version of the manuscript. TG and EH were supported by NEHRP/USGS grant G13AP00047. This research was also supported by the Southern California Earthquake Center (SCEC) under contribution number 12017. SCEC is funded by NSF Cooperative Agreement EAR-0529922 and USGS Cooperative Agreement 07HQAG0008. We would also like to thank the open-source community for many of the programs utilized here (GMT, python, python-basemap, Gimp and the Linux operating system). The here utilized data were obtained from the Southern California Earthquake Data Center (Caltech.Dataset. doi:10.7909/C3WD3xH1).

REFERENCES

Abercrombie, R.E., 1995. Earthquake source scaling relationships from −1 to 5 m_L using seismograms recorded at 2.5 km depth, *J. geophys. Res.,* **100**(B12), 24 015–24 036.

Aki, K., 1981. A probabilistic synthesis of precursory phenomena, in *Earthquake Prediction: An International Review, Maurice Ewing Series,* Vol. 4, pp. 566–574, eds Simpson, D.W. & Richards, P.G., American Geophysical Union.

Allen, C.R., 1957. San Andreas fault zone in San Gorgonio Pass, southern California, *Bull. geol. Soc. Am.,* **68**(3), 315–350.

Allmann, B.P. & Shearer, P.M., 2007. Spatial and temporal stress drop variations in small earthquakes near Parkfield, California, *J. geophys. Res.,* **112**(B4), B04305, doi:10.1029/2006JB004395.

Allmann, B.P. & Shearer, P.M., 2009. Global variations of stress drop for moderate to large earthquakes, *J. geophys. Res.,* **114**(B1), B01310, doi:10.1029/2008JB005821.

Andrews, D.J., 1986. Objective determination of source parameters and similarity of earthquakes of different size, in *Earthquake Source Mechanics,* pp. 259–267.

Baltay, A., Prieto, G. & Beroza, G.C., 2010. Radiated seismic energy from coda measurements and no scaling in apparent stress with seismic moment, *J. geophys. Res.,* **115,** B08314, doi:10.1029/2009JB006736.

Beeler, N.M., Hickman, S.H. & Wong, T.-F., 2001. Earthquake stress drop and laboratory-inferred interseismic strength recovery, *J. geophys. Res.,* **106**(B12), 30 701–30 713.

Behr, W. *et al.*, 2010. Uncertainties in slip-rate estimates for the Mission Creek strand of the southern San Andreas fault at Biskra Palms Oasis, Southern California, *Bull. geol. Soc. Am.,* **122,** 1360–1377.

Ben-Zion, Y. & Ampuero, J.-P., 2009. Seismic radiation from regions sustaining material damage, *Geophys. J. Int.,* **178**(3), 1351–1356.

Blanpied, M.L., Lockner, D.A. & Byerlee, J.D., 1995. Frictional slip of granite at hydrothermal conditions, *J. geophys. Res.,* **100**(B7), 13 045–13 064.

Boatwright, J., Fletcher, J.B. & Fumal, T.E., 1991. A general inversion scheme for source, site, and propagation characteristics using multiply recorded sets of moderate-sized earthquakes, *Bull. seism. Soc. Am.,* **81**(5), 1754–1782.

Brune, J.N., 1970. Tectonic stress and the spectra of seismic shear waves from earthquakes, *J. geophys. Res.,* **75**(26), 4997–5009.

Carena, S., Suppe, J. & Kao, H., 2004. Lack of continuity of the San Andreas fault in Southern California: three-dimensional fault models and earthquake scenarios, *J. geophys. Res.,* **109,** B04313, doi:10.1029/2003JB002643.

Castro, R.R. & Ben-Zion, Y., 2013. Potential signatures of damage-related radiation from aftershocks of the 4 April 2010 (mw 7.2) El Mayor–Cucapah earthquake, Baja California, México, *Bull. seism. Soc. Am.,* **103**(2A), 1130–1140.

Chen, X. & Shearer, P.M., 2013. California foreshock sequences suggest aseismic triggering process, *Geophys. Res. Lett.,* **40**(11), 2602–2607.

Cooke, M.L. & Dair, L.C., 2011. Simulating the recent evolution of the southern big bend of the San Andreas fault, Southern California, *J. geophys. Res.,* **116,** B04405, doi:10.1029/2010JB007835.

Dair, L. & Cooke, M.L., 2009. San Andreas fault geometry through the San Gorgonio Pass, California, *Geology,* **37**(2), 119–122.

Eshelby, J.D., 1957. The determination of the elastic field of an ellipsoidal inclusion, and related problems, *Proc. R. Soc. A,* **241**(1226), 376–396.

Fuis, G.S., Scheirer, D.S., Langenheim, V.E. & Kohler, M.D., 2012. A new perspective on the geometry of the San Andreas fault in Southern California and its relationship to lithospheric structure, *Bull. seism. Soc. Am.,* **102**(1), 236–251.

Goebel, T.H.W., Becker, T.W., Schorlemmer, D., Stanchits, S., Sammis, C., Rybacki, E. & Dresen, G., 2012. Identifying fault hetergeneity through mapping spatial anomalies in acoustic emission statistics, *J. geophys. Res.,* **117,** B03310, doi:10.1029/2011JB008763.

Goebel, T.H.W., Sammis, C.G., Becker, T.W., Dresen, G. & Schorlemmer, D., 2013a. A comparison of seismicity characteristics and fault structure in stick-slip experiments and nature, *Pure appl. Geophys.,* doi:10.1007/s00024-013-0713-7.

Goebel, T.H.W., Schorlemmer, D., Becker, T.W., Dresen, G. & Sammis, C.G., 2013b. Acoustic emissions document stress changes over many seismic cycles in stick-slip experiments, *Geophys. Res. Lett.,* **40,** doi:10.1002/grl.50507.

Graves, R.W., Aagaard, B.T., Hudnut, K.W., Star, L.M., Stewart, J.P. & Jordan, T.H., 2008. Broadband simulations for M_w 7.8 southern San Andreas earthquakes: ground motion sensitivity to rupture speed, *Geophys. Res. Lett.,* **35,** L22302, doi:10.1029/2008GL035750.

Gu, Y. & Wong, T.-F., 1991. Effects of loading velocity, stiffness, and inertia on the dynamics of a single degree of freedom spring-slider system, *J. geophys. Res.,* **96**(B13), 21 677–21 691.

Hanks, T.C., 1979. *b* values and ω-γ seismic source models: Implications for tectonic stress variations along active crustal fault zones and the estimation of high-frequency strong ground motion, *J. geophys. Res.,* **84**(B5), 2235–2242.

Hanks, T.C. & McGuire, R.K., 1981. The character of high-frequency strong ground motion, *Bull. seism. Soc. Am.,* **71**(6), 2071–2095.

Hanks, T.C. & Thatcher, W., 1972. A graphical representation of seismic source parameters, *J. geophys. Res.,* **77**(23), 4393–4405.

Harrington, R.M. & Brodsky, E.E., 2009. Source duration scales with magnitude differently for earthquakes on the San Andreas Fault and on secondary faults in Parkfield, California, *Bull. seism. Soc. Am.,* **99**(4), 2323–2334.

Hauksson, E., 2015. Average stress drops of southern California earthquakes in the context of crustal geophysics: implications for fault zone healing, *Pure appl. Geophys.,* **172**(5), 1359–1370.

Hauksson, E., Yang, W. & Shearer, P.M., 2012. Waveform relocated earthquake catalog for Southern California (1981 to June 2011), *Bull. seism. Soc. Am.,* **102**(5), 2239–2244.

He, C., Wong, T.-F. & Beeler, N.M., 2003. Scaling of stress drop with recurrence interval and loading velocity for laboratory-derived fault strength relations, *J. geophys. Res.,* **108**(B1), doi:10.1029/2002JB001890.

Heaton, T.H., Tajima, F. & Mori, A.W., 1986. Estimating ground motions using recorded accelerograms, *Surv. Geophys.,* **8**(1), 25–83.

Ide, S. & Beroza, G.C., 2001. Does apparent stress vary with earthquake size?, *Geophys. Res. Lett.,* **28**(17), 3349–3352.

Kanamori, H., 1986. Rupture process of subduction-zone earthquakes, *Annual Review of Earth and Planetary Sciences,* **14**(1), 293–322.

Kanamori, H., Mori, J., Hauksson, E., Heaton, T.H., Hutton, L.K. & Jones, L.M., 1993. Determination of earthquake energy release and m_l using terrascope, *Bull. seism. Soc. Am.,* **83**(2), 330–346.

Kaneko, Y. & Shearer, P.M., 2014. Seismic source spectra and estimated stress drop derived from cohesive-zone models of circular subshear rupture, *Geophys. J. Int.,* **197**(2), 1002–1015.

Knopoff, L., 1958. Energy release in earthquakes, *Geophys. J. Int.,* **1**(1), 44–52.

Kwiatek, G., Plenkers, K. & Dresen, G., 2011. Source parameters of picoseismicity recorded at Mponeng deep gold mine, South Africa: implications for scaling relations, *Bull. seism. Soc. Am.,* **101**(6), 2592–2608.

Langenheim, V.E., Jachens, R.C., Matti, J.C., Hauksson, E., Morton, D.M. & Christensen, A., 2005. Geophysical evidence for wedging in the San Gorgonio Pass structural knot, southern San Andreas fault zone, southern California, *Bull. geol. Soc. Am.,* **117**(11–12), 1554–1572.

Lin, Y.-Y., Ma, K.-F. & Oye, V., 2012. Observation and scaling of microearthquakes from the Taiwan Chelungpu-fault borehole seismometers, *Geophys. J. Int.,* **190**(1), 665–676.

Madariaga, R., 1976. Dynamics of an expanding circular fault, *Bull. seism. Soc. Am.,* **66**(3), 639–666.

Magistrale, H. & Sanders, C., 1996. Evidence from precise earthquake hypocenters for segmentation of the San Andreas fault in San Gorgonio Pass, *J. geophys. Res.,* **101**(B2), 3031–3044.

Matti, J., Morton, D. & Cox, B., 1992. The San Andreas fault system in the vicinity of the central Transverse Ranges province, Southern California, *U.S. Geol. Surv., Reston, Va.,* **40,** 92–354.

McGarr, A., Spottiswoode, S.M. & Gay, N.C., 1979. Observations relevant to seismic driving stress, stress drop and efficiency, *J. geophys. Res.,* **84,** 2251–2261.

McGill, S.F., Owen, L.A., Weldon, R.J. & Kendrick, K.J., 2013. Latest Pleistocene and Holocene slip rate for the San Bernardino strand of the San Andreas fault, Plunge Creek, Southern California: implications for strain partitioning within the southern San Andreas fault system for the last ~ 35 ky, *Bull. geol. Soc. Am.,* **125**(1–2), 48–72.

McLaskey, G.C., Thomas, A.M., Glaser, S.D. & Nadeau, R.M., 2012. Fault healing promotes high-frequency earthquakes in laboratory experiments and on natural faults, *Nature,* **491**(7422), 101–104.

Nadeau, R.M. & Johnson, L.R., 1998. Seismological studies at parkfield VI: moment release rates and estimates of source parameters for small repeating earthquakes, *Bull. seism. Soc. Am.,* **88**(3), 790–814.
Nazareth, J.J. & Hauksson, E., 2004. The seismogenic thickness of the southern California crust, *Bull. seism. Soc. Am.,* **94**(3), 940–960.
Nicholson, C., Seeber, L., Williams, P. & Sykes, L.R., 1986. Seismicity and fault kinematics through the Eastern Transverse ranges, California: block rotation, strike-slip faulting and low-angle thrusts, *J. geophys. Res.,* **91**(B5), 4891–4908.
Orozco, A. & Yule, D., 2003. Late Holocene slip rate for the San Bernardino strand of the San Andreas Fault near Banning, California, *Seism. Res. Lett.,* **74**(2), 237.
Oth, A., 2013. On the characteristics of earthquake stress release variations in Japan, *Earth planet. Sci. Lett.,* **377,** 132–141.
Prieto, G.A., Shearer, P.M., Vernon, F.L. & Kilb, D., 2004. Earthquake source scaling and self-similarity estimation from stacking P and S spectra, *J. geophys. Res.,* **109,** B08310, doi:10.1029/2004JB003084.
Rubin, A.M. & Ampuero, J.-P., 2005. Earthquake nucleation on (aging) rate and state faults, *J. geophys. Res.,* **110**(B11), doi:10.1029/2005JB003686.
Sammis, C.G. & Rice, J.R., 2001. Repeating earthquakes as low-stress-drop events at a border between locked and creeping fault patches, *Bull. seism. Soc. Am.,* **91**(3), 532–537.
Sammonds, P. & Ohnaka, M., 1998. Evolution of microseismicity during frictional sliding, *Geophys. Res. Lett.,* **25,** 699–702.
Sato, T. & Hirasawa, T., 1973. Body wave spectra from propagating shear cracks, *J. Phys. Earth,* **21**(4), 415–431.
Scholz, C.H., 1988. The brittle-plastic transition and the depth of seismic faulting, *Geologische Rundschau,* **77**(1), 319–328.
Shearer, P., Hauksson, E. & Lin, G., 2005. Southern California hypocenter relocation with waveform cross-correlation, part 2: results using source-specific station terms and cluster analysis, *Bull. seism. Soc. Am.,* **95**(3), 904–915.
Shearer, P.M., 2009. *Introduction to Seismology,* Cambridge Univ. Press.
Shearer, P.M., Prieto, G.A. & Hauksson, E., 2006. Comprehensive analysis of earthquake source spectra in southern California, *J. geophys. Res.,* **111,** B06303, doi:10.1029/2005JB003979.
Thompson, B.D., Young, R.P. & Lockner, D.A., 2005. Observations of pre-monitory acoustic emission and slip nucleation during a stick slip experiment in smooth faulted westerly granite, *Geophys. Res. Lett.,* **32,** doi:10.1029/2005GL022750.
Tse, S.T. & Rice, J.R., 1986. Crustal earthquake instability in relation to the depth variation of frictional slip properties, *J. geophys. Res.,* **91**(B9), 9452–9472.
Walter, W.R., Mayeda, K., Gok, R. & Hofstetter, A., 2006. The scaling of seismic energy with moment: simple models compared with observations, in *Earthquakes: Radiated Energy and the Physics of Faulting,* pp. 25–41, eds Abercrombie, R. *et al.*, American Geophysical Union.
Warren, L.M. & Shearer, P.M., 2000. Investigating the frequency dependence of mantle Q by stacking P and PP spectra, *J. geophys. Res.,* **105**(B11), 25 391–25 402.
Weldon, R.J. & Sieh, K.E., 1985. Holocene rate of slip and tentative recurrence interval for large earthquakes on the San Andreas fault, Cajon Pass, southern California, *Bull. geol. Soc. Am.,* **96**(6), 793–812.
Yang, W. & Hauksson, E., 2011. Evidence for vertical partitioning of strike-slip and compressional tectonics from seismicity, focal mechanisms, and stress drops in the east Los Angeles basin area, California, *Bull. seism. Soc. Am.,* **101**(3), 964–974.
Yang, W., Peng, Z. & Ben-Zion, Y., 2009. Variations of strain-drops of aftershocks of the 1999 İzmit and Düzce earthquakes around the Karadere-Düzce branch of the North Anatolian Fault, *Geophys. J. Int.,* **177**(1), 235–246.
Yang, W., Hauksson, E. & Shearer, P.M., 2012. Computing a large refined catalog of focal mechanisms for southern California (1981–2010): Temporal stability of the style of faulting, *Bull. seism. Soc. Am.,* **102**(3), 1179–1194.
Yule, D. & Sieh, K., 2003. Complexities of the San Andreas fault near San Gorgonio Pass: implications for large earthquakes, *J. geophys. Res.,* **108,** doi:10.1029/2001JB000451.
Yule, D., Fumal, T., McGill, S. & Seitz, G., 2001. Active tectonics and paleoseismic record of the San Andreas fault, Wrightwood to Indio: working toward a forecast for the next 'Big Event', in *Geologic Excursions in the California Deserts and Adjacent Transverse Ranges,* pp. 91–126, eds Dunne, G. & Cooper, J., Geological Society of America Fieldtrip Guidebook and Volume prepared for the Joint Meeting of the Cordilleran Section GSA and Pacific Section AAPG.

SUPPORTING INFORMATION

Additional Supporting Information may be found in the online version of this paper:

Table S1. Parameter choices and frequency bands used to compute spectra, corner frequencies and stress drops.
Table S2. Difference in stress-drop estimates (diff. $\Delta\sigma$) and statistical significance for a non-parametric test and tests assuming log-normally distributed data. Population types refer to the two different populations that are compared: low/high $\Delta\sigma$ region: A low and high stress-drop region (see Fig. 3b in main manuscript); normal/strike-slip foc. mech.: predominantly normal vs. strike-slip focal mechanisms; and strike-slip/thrust foc. mech.: strike-slip vs. thrust focal mechanisms; 7/15 km depth: Stress drop estimates at 7 and 15 km depth; 56/78 km distance from Cajon pass: Stress-drop estimates along the San Andreas fault zone at 56 and 78 km distance from Cajon Pass.
Figure S1. Schematic image of ray-paths of event waveforms recorded at different stations (a), and different events within a small region recorded at the same station (b). The recorded waveforms are a convolution of source (e_i), path (t_{ij}) and site (s_j) contributions.
Figure S2. Source spectra stacked over events within 0.2 magnitude bins (grey curves) and corresponding Brune-type spectral fits (blue dashed lines). The red curve represents the regional average empirical Green's function used to correct high frequency contributions and the black dashed line highlights the line of constant stress drop for which $M_0 \propto f_c^{-3}$. This relationship is also used to correct for differences in moments by shifting along f^{-3} until the low frequency moments coincide (b).
Figure S3. Average path terms (solid lines) stacked within 2 s bins and empirical correction function (ECS). The ECS is computed by averaging the misfit between an exponential attenuation model with $Q_P = 550$ (curves, coloured with travel-time), analogous to Shearer *et al.* (2006). The ECS removes the ambiguity with respect to a constant log spectrum that could be added and subtracted from any pair of terms in eq. (1) in the main manuscript, similar to the EGF used to correct the source spectra.
Figure S4. Example of four events with strongly varying stress drops, i.e. similar relative moments (low frequency content) but different corner frequencies. The grey curve highlights the average source spectra for all stations and the coloured areas in the background show the density of spectra from individual stations, so that warmer colors correspond to higher density of spectra. The blue dashed lines show the Brune-type spectral fits and grey, dashed curves represent the confidence bounds of the spectral density estimates as a function of frequency. The grey, shaded frequency range above 20 Hz was not included during the computation of the spectral fits.
Figure S5. Changes in root-mean-square misfit between observed and modeled source spectra for different stress drop values. The round markers are colored according to corner frequency. The square markers show the average rms-values for different stress drop magnitudes.

Figure S6. Histograms of stress drop values for different input parameters, SNR, and N_{spec} of the source inversions. The parameters are displayed in the upper left of each subplot together with the mean stress drops which showed only small variations. The top frame depicts the input parameters used for the analysis in the main manuscript.

Figure S7. Corner frequency as a function of seismic moment for a less (red markers) and a highly (blue markers) restrictive selection of spectral quality criteria. The latter results in an exclusion of many small magnitude events from the analysis but also reduces the scatter substantially, especially, for spectra with small seismic moments. The corresponding mean stress drops (red and blue, dashed lines) change by a factor of ∼1.2–2 while preserving the difference between low and high stress drop regions.

Figure S8. Variations in stress drops (green) and misfit (red) between source spectra and Brune-type model as function of N_{spec} (a) and SNR (b). The dashed lines depict results for a low stress drop region and solid lines for a high stress drop region.

Figure S9. Same as Fig. 8 but now for a larger region. The absolute stress drops decrease due to smoothing over larger areas, however, the difference between low and high stress drop region remains.

Figure S10. Smoothed spatial variations of stress drops computed from spectra with SNR ≥ 6 and $N_{spec} \geq 12$. The overall pattern of low and high stress drop regions is similar to that in Fig. 3 of the main manuscript.

Figure S11. Variations in stress drops as a function of depth. The figure is the same as Fig. 7 in the main manuscript with added stress drop results for the high quality dataset (black dots).

Figure S12. Variations in stress drops as a function of focal mechanism type. The figure is the same as Fig. 9 in the main manuscript with added stress drop results for the high quality dataset (open circles).

Figure S13. Variations in stress drops as a function of geological slip rates. The figure is the same as Fig. 10 in the main manuscript with added stress drop results for the high quality dataset (open circles).

Figure S14. Comparison between different parametric and non-parametric tests to determine if variations in stress-drop distributions are statistically significant (see text for details). The shown results are for synthetic log-normal distributions with mean values between 1–10 MPa. $\Delta\sigma$ is the corresponding parameter that controls the changes in scale and $\Delta \log(\mu)$ specifies the difference in mean of the log-transformed data (here log refers to the natural logarithm). (http://gji.oxfordjournals.org/lookup/suppl/doi:10.1093/gji/ggv160/-/DC1)